

LWGANet: A Lightweight Group Attention Backbone for Remote Sensing Visual Tasks

Wei Lu, Si-Bao Chen*, *Member, IEEE*, Chris H. Q. Ding, Jin Tang, and Bin Luo, *Senior Member, IEEE*

Abstract— Remote sensing (RS) visual tasks have gained significant academic and practical importance. However, they encounter numerous challenges that hinder effective feature extraction, including the detection and recognition of multiple objects exhibiting substantial variations in scale within a single image. While prior dual-branch or multi-branch architectural strategies have been effective in managing these object variances, they have concurrently resulted in considerable increases in computational demands and parameter counts. Consequently, these architectures are rendered less viable for deployment on resource-constrained devices. Contemporary lightweight backbone networks, designed primarily for natural images, frequently encounter difficulties in effectively extracting features from multi-scale objects, which compromises their efficacy in RS visual tasks. This article introduces LWGANet, a specialized lightweight backbone network tailored for RS visual tasks, incorporating a novel lightweight group attention (LWGA) module designed to address these specific challenges. The LWGA module, tailored for RS imagery, adeptly harnesses redundant features to extract a wide range of spatial information, from local to global scales, without introducing additional complexity or computational overhead. This facilitates precise feature extraction across multiple scales within an efficient framework. LWGANet was rigorously evaluated across twelve datasets, which span four crucial RS visual tasks: scene classification, oriented object detection, semantic segmentation, and change detection. The results confirm LWGANet’s widespread applicability and its ability to maintain an optimal balance between high performance and low complexity, achieving state-of-the-art results across diverse datasets. LWGANet emerged as a novel solution for resource-limited scenarios requiring robust RS image processing capabilities. The code is available at <https://github.com/lwCVer/LWGANet>.

Index Terms—Backbone network, remote sensing (RS), lightweight, classification, detection, segmentation, change detection, group attention, feature decoupling.

I. INTRODUCTION

IN recent years, remote sensing (RS) optical image recognition technology, based on deep learning, has significantly influenced areas such as environmental monitoring, urban planning, and agricultural yield assessment. This technique covers a wide geographical area and captures rich surface

Corresponding author (*): Si-Bao Chen. This work was supported in part by the NSFC Key Project of Joint Fund for Enterprise Innovation and Development under Grant U20B2068, and in part by the National Natural Science Foundation of China under Grant 61976004.

Wei Lu, Si-Bao Chen, Jin Tang, and Bin Luo are with the MOE Key Laboratory of ICSP, IMIS Laboratory of Anhui, Anhui Provincial Key Laboratory of Multimodal Cognitive Computation, Zenmorn-AHU AI Joint Laboratory, School of Computer Science and Technology, Anhui University, Hefei 230601, China (e-mail: 2858191255@qq.com; sbchen@ahu.edu.cn; tj@ahu.edu.cn; luobin@ahu.edu.cn).

Chris H. Q. Ding is with the School of Data Science (SDS), Chinese University of Hong Kong, Shenzhen 518172, China (e-mail: chrisding@cuhk.edu.cn).

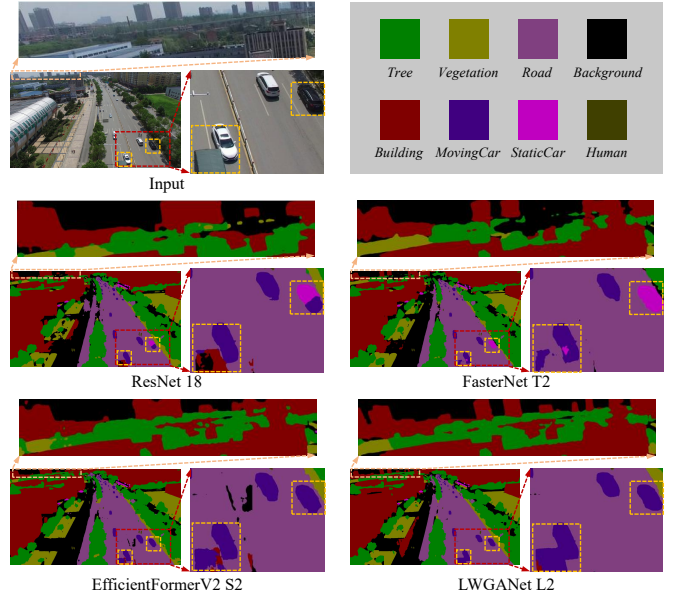


Fig. 1: Visual results on UAVid test set [1]. The Unet-Former [2] was used as the segmentation head.

features. However, there are numerous challenges in the processing and analyses of RS images, in particular the large-scale variations in object sizes due to the spatial resolution and shot angles of satellites, and diverse objects. These variations in object size greatly increase the difficulty of object recognition and detection, which affects the accuracy and reliability of the recognition results and poses the pressing technical challenges in the RS optical visual tasks.

The primary obstacles in multi-scale object recognition and detection have revolved around efficiently processing and distinguishing objects of various sizes. This requires recognition or detection systems to accommodate a broad spectrum of variations, from minute details to larger structures, while preserving sensitivity and discerning resolution toward object attributes. The underlying complexity stems from the fact that objects across large-scale variations may require diverse feature extraction and identification approaches. Traditional recognition and detection models typically struggle to address this size diversity.

To address the aforementioned challenges, researchers propose various solutions such as multi-scale feature analyses and multi-branch structural feature extraction techniques. The multi-scale feature analyses [3], [4], [5] establish the multi-level feature pyramid networks (FPN) to analyze the expression of objects at different scales in detail, aiming to

improve recognition accuracy and adaptability. Meanwhile, multi-branch structural feature extraction techniques [6], [7], [8] process object features at different scales by parallelly connecting multiple branch modules, utilizing the unique advantages of each branch module to extract the features of the large-scale variational objects for effective detection and recognition. However, these methods still have limitations in practical applications. For instance, multi-scale architectures may not comprehensively characterize the features of various object sizes at a particular scale, and multi-branch architectures exacerbate the difficulty of lightweight RS visual tasks due to the increased parameters and computational load.

Moreover, traditional lightweight networks typically fail to account for specific characteristics of RS images, such as multiple objects and significant variations in object size, which leads to inadequate recognition and detection capabilities. Consequently, the process of lightweighting in RS visual tasks lags significantly compared to visual tasks in natural scenes. As illustrated in Fig. 1, the segmentation results from the UAVid test set [1] demonstrate distinct performance characteristics across different models. EfficientFormerV2 [9], utilizing a global attention mechanism, excels in delineating moving cars. FasterNet [10] struggles to accurately segment these vehicles due to the lack of comprehensive contextual information. The local convolution employed by FasterNet captures the intricate details of building structures, but the reliance of EfficientFormerV2 on the global attention mechanism limits its effectiveness in this domain.

To overcome these challenges, we propose LWGANet, a novel lightweight backbone network specifically designed for the RS visual tasks. LWGANet has demonstrated superior performance on multiple RS visual tasks, demonstrating its advantages in terms of parameter efficiency and computational efficiency, and showing broad applicability to tasks such as scene classification, oriented object detection, semantic segmentation, and change detection. As depicted in Fig. 1, LWGANet adeptly segments both mobile and stationary cars by harnessing semantic context effectively. Moreover, it demonstrates superiority in extracting fine-grained details, resulting in exceptional segmentation of buildings.

Lightweight group attention (LWGA) mechanism, the core feature extraction module within the LWGANet, is engineered to enhance the representation of multi-scale objects within RS imagery. The module partitions the input feature map into distinct submodules without augmenting its spatial dimensions, thus achieving a cooperative balance between multi-scale feature extraction and lightweight computational efficiency.

The LWGA module capitalizes on the inherent redundancy [11], [12], [10] present within the feature map, by processing each partition via multiple feature extraction techniques. These include point attention, local attention, medium-range attention, and global attention, which are designed to refine the focus on objects exhibiting large-scale variations. Subsequently, the extracted features are fused to optimize the feature representation, effectively mitigating the challenges associated with multi-scale object recognition during the lightweight feature extraction phase.

To effectively extract exceedingly small features, LWGA

module incorporates a gate point attention (GPA) submodule. By leveraging point attention principles, the GPA prioritizes features from diminutive objects, preserving subtle distinctions typically overlooked by traditional methods.

To extract local features, LWGA module integrates a regular local attention (RLA) submodule. Drawing on the inherent capabilities of standard convolutions, the RLA module excels in extracting local features with precision and efficiency.

For medium-scale object features within lightweight frameworks, LWGA introduces a sparse medium-range attention (SMA) submodule. This module incorporates contextual information to effectively preserve essential features of medium-sized objects with irregular structures.

Additionally, to enhance overall feature representations within lightweight constraints, the LWGA module integrates a sparse global attention (SGA) submodule. This submodule excels at associating long-range features and provides robust global summarization capabilities, with modifications tailored for resource-constrained environments.

The LWGA module both optimizes the network's ability to discern intricate details across various sizes and ensures that the computational demands remain within manageable limits, supporting the constraints of resource-constrained environments. These findings provide new perspectives and tools for theoretical research and practical applications in RS optical image processing, and are expected to promote the development of lightweight RS technology.

In summary, the contributions of this study are as follows:

- 1) A lightweight group attention module, which is named LWGA module, is proposed to efficiently extract features of multi-scale objects in a lightweight setting.
- 2) A lightweight backbone network LWGANet is proposed for multiple RS visual tasks.
- 3) Extensive and rigorous experiments on 12 datasets covering four prominent RS visual tasks: scene classification, object detection, semantic segmentation, and change detection, are conducted to validate the effectiveness and versatility of LWGANet.

II. RELATED WORK

A. Backbones

In the past decade, convolutional neural networks (CNNs) [13] have significantly advanced the field of computer vision (CV), driving improvements in various applications, including image classification, object detection, and segmentation. As the demand for efficient models capable of operating on resource-constrained devices, such as smartphones and embedded systems, has increased, researchers have developed lightweight architectures. These architectures aim to mitigate model complexity and reduce latency through various strategies, including compact model design [14], which focus on minimizing the number of parameters while maintaining performance. Techniques such as pruning [15] further enhance efficiency by removing redundant weights, while structural reparameterization [16] enables dynamic adjustment of network structures to optimize performance. The advent of automated model design through network architecture search [17] has

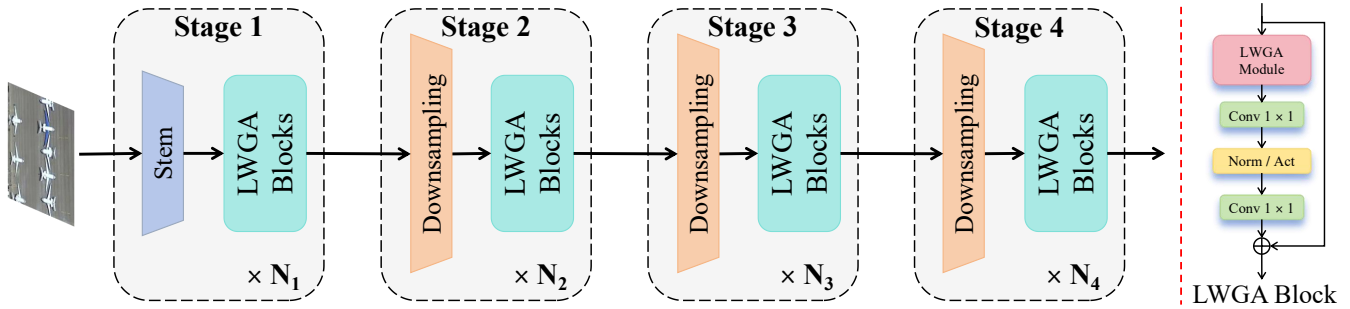


Fig. 2: Overview of the LWGANet. It encompasses four stages, each featuring dimensions of $\frac{H}{4} \times \frac{W}{4} \times C$, $\frac{H}{8} \times \frac{W}{8} \times 2C$, $\frac{H}{16} \times \frac{W}{16} \times 4C$, and $\frac{H}{32} \times \frac{W}{32} \times 8C$, where H , W , and C denote the feature height, width, and channel dimension, respectively.

further transformed the development of lightweight networks, allowing for the discovery of optimal configurations tailored to specific tasks.

Since the introduction of Vision Transformer (ViT) [18] to the CV landscape in 2020, there has been a surge of interest, resulting in numerous variants aimed at improving performance across various domains. Enhancements such as pyramid structures [19] facilitate multi-scale feature extraction, while local attention mechanisms [20] enable the model to focus on relevant local regions within the input data. Additionally, the development of lightweight model [21] highlights the ongoing effort to balance computational efficiency with model accuracy on visual tasks.

This growing interest has also catalyzed exploration into alternative architectures, including multilayer perceptron [22] and graph convolutional network [23], which offer unique advantages for specific tasks and datasets. Such developments underscore the continuous evolution of backbone networks in CV, addressing the challenges posed by increasingly complex data and application requirements.

B. RS Visual Tasks

Remote sensing (RS) image analysis and related visual tasks are critical areas of study for Earth scientists, providing insights into environmental monitoring, land use classification, and disaster management. Scene classification [24] exemplifies these tasks, with researchers employing a variety of datasets [25], [26] to explore advancements in classification methodologies. For example, [27] proposed a lightweight CNN model based on MobileNet V2 [28] specifically designed for scene classification in high spatial resolution RS images, demonstrating the effectiveness of lightweight architectures in this domain. Similar efforts to develop efficient models can be found in [29], [30], each contributing to the growing body of research focused on enhancing performance while maintaining resource efficiency.

Despite these advancements, the applicability of existing lightweight networks to downstream tasks such as object detection [31] and segmentation [32] remains uncertain. The current lack of specialized backbone networks designed explicitly for lightweight RS visual tasks has led to a reliance on traditional visual backbones, such as MobileNet V2 and ResNet-18 [33]. This dependency restricts the potential for performance improvements in lightweight RS visual tasks,

highlighting the need for further research into tailored architectures that can effectively balance efficiency and accuracy in this critical area of study.

III. APPROACH

This section provides a detailed analyses of LWGANet architecture in Section III-A, which is specifically for efficient RS visual tasks on resource-constrained devices. Furthermore, the implementation details of LWGA module within the network, as outlined in Section III-B.

A. Architectural Configurations of LWGANet

As illustrated in Fig. 2, the architecture of LWGANet is structured hierarchically into four stages to facilitate scalable feature extraction, with reductions in dimensionality by factors of $1/4$, $1/8$, $1/16$, and $1/32$ at each stage. The architecture consists of models L0, L1, and L2 with initial stem layer channel counts of 32, 64, and 96, respectively.

The first stage of LWGANet starts with a convolution at a stride of four (stem layer), followed by a sequence of LWGA blocks denoted as $\times N_i$, where N_i indicates the number of LWGA blocks in the i^{th} stage. The detailed configurations (N_1, N_2, N_3, N_4) are depicted in Table I. Each subsequent stage consists of a downsampling process and additional LWGA blocks, whose outputs are eventually fed to a task-specific decoder. The downsampling utilizes the DRFD module [34], which merges convolutional and max-pooling methods to optimally preserve fine details and small-scale features. More architecture details can be found in Table I.

In the LWGA block, as depicted in the right side of Fig. 2, the input feature map \mathbf{X} undergoes processing through LWGA module, yielding the feature \mathbf{Y} . Subsequently, a channel multilayer perceptron (CMLP) module is applied to feature \mathbf{Y} . CMLP module is constructed as follows: initially, a convolution layer is applied with parameters $(I = C, O = 2C, K = 1, S = 1)$, followed by batch normalization (BN) and activation function (Act), resulting in feature map \mathbf{Y}' . Then, \mathbf{Y}' undergoes convolution with parameters $(I = 2C, O = C, K = 1, S = 1)$, producing feature map \mathbf{Y}'' . The output feature map is obtained as follows:

$$\begin{aligned} CMLP &= Conv(Act(BN(Conv(\mathbf{X}))), \\ out &= \mathbf{X} + BN(drop(CMLP(\mathbf{X}))), \end{aligned} \quad (1)$$

where $drop$ represents dropout.

TABLE I: Architecture configurations of LWGANet.

Stage	Downs. rate	Model layers	Number of input/output channels		
			L0	L1	L2
1	$\frac{H}{4} \times \frac{W}{4}$	<i>Stem Layer</i>	3/32	3/64	3/96
		$[LWGA \text{ Block}] \times N_1$	32/32	64/64	96/96
2	$\frac{H}{8} \times \frac{W}{8}$	<i>DRFD Module</i>	32/64	64/128	96/192
		$[LWGA \text{ Block}] \times N_2$	64/64	128/128	192/192
3	$\frac{H}{16} \times \frac{W}{16}$	<i>DRFD Module</i>	64/128	128/256	192/384
		$[LWGA \text{ Block}] \times N_3$	128/128	256/256	384/384
4	$\frac{H}{32} \times \frac{W}{32}$	<i>DRFD Module</i>	128/256	256/512	384/768
		$[LWGA \text{ Block}] \times N_4$	256/256	512/512	768/768
SMA distance			[11, 11, 11, 11]	[11, 11, 11, 11]	[11, 11, 11, 11]
Number of Block			[1, 2, 4, 2]	[1, 2, 4, 2]	[1, 4, 4, 2]
Activation			<i>GELU</i>	<i>GELU</i>	<i>ReLU</i>
Dropout			0.0	0.1	0.1
Parameters			1.72M	5.90M	13.0M
FLOPs			0.186G	0.709G	1.87G

B. LWGA Module

The LWGA module serves as the primary feature extraction component of LWGANet, depicted in Fig. 3. LWGA module processes the input feature map $\mathbf{X} \in \mathbb{R}^{H \times W \times C}$ by partitioning it into four equal segments $\{\mathbf{X}_1, \mathbf{X}_2, \mathbf{X}_3, \mathbf{X}_4\}$, where $\mathbf{X}_i \in \mathbb{R}^{H \times W \times \frac{C}{4}}$. Here, \mathbf{X} represents the tensor, $\mathbb{R}^{H \times W \times C}$ denotes the real number field, and H , W , and C represent the feature height, width, and number of channels, respectively.

1) *TGFI Module*: To alleviate the global attention computational burden and enlarged receptive field, we introduce the top-k global feature interaction (TGFI) module. As depicted in Fig. 3, the primary function of the TGFI module is to extract the top k salient features from an input feature map $\mathbf{X} \in \mathbb{R}^{H \times W \times C}$ and to form a new feature map $\mathbf{Y} \in \mathbb{R}^{\frac{H}{n} \times \frac{W}{n} \times C}$, where n is determined by the number of top-k features. This process also retains the coordinate location information \mathcal{L}_p . Subsequently, global feature interactions are computed for each feature point in \mathbf{Y} , establishing global relationships among the top k salient features, resulting in feature map \mathbf{Z} . Finally, the feature dimensions of \mathbf{Z} are restored using the coordinate location information \mathcal{L}_p , yielding the output feature map \mathbf{out} , i.e., $\mathbf{Z} \in \mathbb{R}^{\frac{H}{n} \times \frac{W}{n} \times C} \xrightarrow{\mathcal{L}_p} \mathbf{out} \in \mathbb{R}^{H \times W \times C}$.

2) *GPA Module*: As shown by GPA in Fig. 4, the GPA module processes the feature \mathbf{X}_1 . Initially, its channels are expanded through a $(I = C/4, O = C, K = 1, S = 1)$ convolution, resulting in \mathbf{X}'_1 . Here, I , O , K , and S represent the input channels, output channels, convolution kernel size, and stride, respectively. Subsequent steps include BN, activation function with GELU [35] (replacing L2 with ReLU [36]), and restoration of channels via a $(I = C, O = C/4, K = 1, S = 1)$ convolution to obtain \mathbf{X}''_1 . Applying a sigmoid operation to \mathbf{X}''_1 generates the attention map \mathcal{A}_1 . The output feature \mathbf{R}_1 is then obtained by combining \mathbf{X}_1 and the element-wise product of \mathcal{A}_1 and \mathbf{X}_1 , i.e., $\mathbf{R}_1 = \mathbf{X}_1 + \mathcal{A}_1 \cdot \mathbf{X}_1$.

3) *RLA Module*: As shown by RLA in Fig. 4, the RLA module processes the feature \mathbf{X}_2 , functioning similarly to

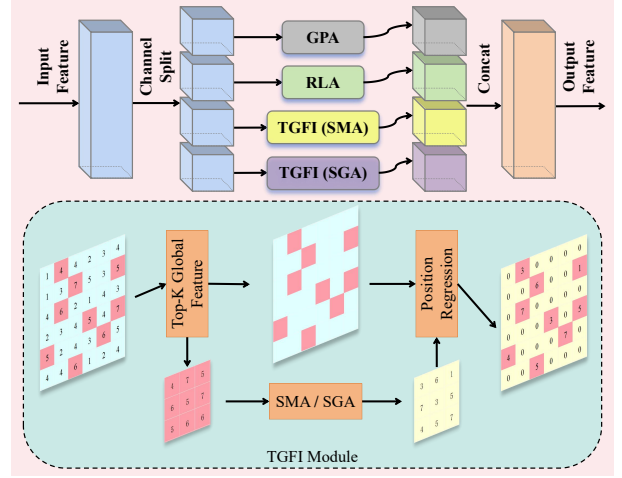


Fig. 3: Illustration of LWGA module.

standard convolutions. \mathbf{X}_2 undergoes a $(I = C/4, O = C/4, K = 3, S = 1, P = 1)$ convolution, with P denoting padding, to generate \mathbf{X}'_2 . Following this, BN and activation function are applied to produce the output feature \mathbf{R}_2 .

4) *SMA Module*: As shown by SMA in Fig. 4, the SMA module takes the feature \mathbf{X}_3 as input. Initially, the TGFI module reduces its feature size to $\mathbf{X}'_3 \in \mathbb{R}^{\frac{H}{3} \times \frac{W}{3} \times \frac{C}{4}}$, thereby enhancing its receptive field meanwhile preserving the original position coordinates \mathcal{L}_p . The resulting SMA processing \mathbf{X}'_3 generates \mathcal{A}'_3 , formulated to integrate contextual information, as shown below:

$$\begin{aligned} \mathcal{A}_{ij} = & \sum_{n=0}^{n=\frac{L-1}{2}} \alpha_{(i \pm n)j} \cdot x_{(i \pm n)j} + \sum_{n=0}^{n=\frac{L-1}{2}} \alpha_{(i \pm n)(j \pm n)} \cdot x_{(i \pm n)(j \pm n)} \\ & + \sum_{n=0}^{n=\frac{L-1}{2}} \alpha_{i(j \pm n)} \cdot x_{i(j \pm n)} + \sum_{n=0}^{n=\frac{L-1}{2}} \alpha_{(i \mp n)(j \pm n)} \cdot x_{(i \mp n)(j \pm n)}, \end{aligned} \quad (2)$$

where x_{ij} denotes the feature at position (i, j) , and α_{ij} represents the coefficient of relation with x_{ij} , a learnable parameter. In this study, L is set to 11. After enhancing \mathcal{A}'_3 feature size with TGFI module interpolation to match the size of \mathbf{X}_3 , resulting in \mathcal{A}_3 , i.e., $\mathcal{A}'_3 \in \mathbb{R}^{\frac{H}{3} \times \frac{W}{3} \times \frac{C}{4}} \xrightarrow{\mathcal{L}_p} \mathcal{A}_3 \in \mathbb{R}^{H \times W \times \frac{C}{4}}$. The output feature \mathbf{R}_3 is then obtained as the element-wise product of \mathbf{X}_3 and \mathcal{A}_3 , i.e., $\mathbf{R}_3 = \mathcal{A}_3 \cdot \mathbf{X}_3$.

5) *SGA Module*: As shown by SGA in Fig. 4, the SGA module processes the feature \mathbf{X}_4 , employing distinct strategies tailored to different stages to ensure lightweight processing.

For stages 1 and 2, where the feature size is $1/4$ and $1/8$ compared to the original input size, respectively. SGA module reduces the feature size with TGFI module to obtain feature map $\mathbf{X}'_4 \in \mathbb{R}^{\frac{H}{2} \times \frac{W}{2} \times \frac{C}{4}}$ and position coordinates \mathcal{L}_p . Subsequent steps involve simple feature extraction via a $(I = C/4, O = C/4, K = 5, S = 1, P = 2, G = C/4)$ convolution, where G represents groups, yielding \mathbf{X}''_4 . A dilated convolution with parameters $(I = C/4, O = C/4, K = 7, S = 1, P = 9, G = C/4, D = 3)$ —where D denotes the dilation coefficient—replaces the global attention mechanism. Acting on \mathbf{X}''_4 , this dilated convolution generates the attention map \mathcal{A}_{412} . The resulting feature $\mathbf{R}'_4 = \mathcal{A}_{412} \cdot \mathbf{X}'_4$. Finally, \mathbf{R}'_4

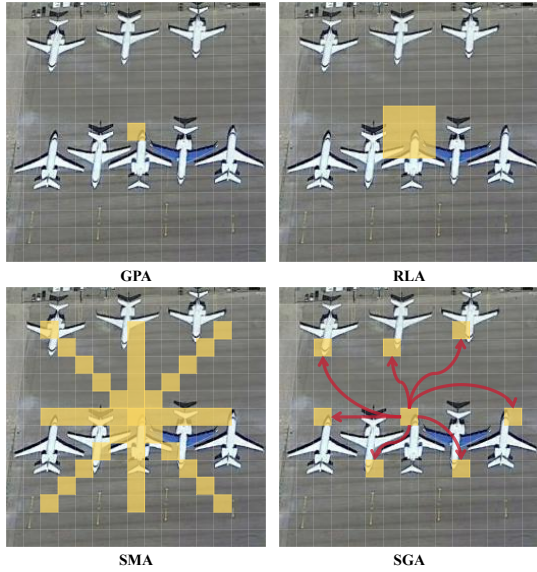


Fig. 4: Illustration of various attention modules.

is restored to its original size using the position coordinates \mathcal{L}_p , i.e., $\mathbf{R}'_4 \in \mathbb{R}^{\frac{H}{2} \times \frac{W}{2} \times \frac{C}{4}} \xrightarrow{\mathcal{L}_p} \mathbf{R}''_4 \in \mathbb{R}^{H \times W \times \frac{C}{4}}$. The output feature \mathbf{R}_4 is obtained by adding \mathbf{R}''_4 to \mathbf{X}_4 , followed by BN, i.e., $\mathbf{R}_4 = BN(\mathbf{R}''_4 + \mathbf{X}_4)$.

For stage 3, we reduce the feature size with TGFI module to obtain $\mathbf{X}'_4 \in \mathbb{R}^{\frac{H}{2} \times \frac{W}{2} \times \frac{C}{4}}$ and position coordinates \mathcal{L}_p . The commonly used mechanism of vision attention [18] with a head_num of 4, denoted as \mathcal{A}_{43} , applied to \mathbf{X}'_4 . This yields the feature \mathbf{R}'_4 , which $\mathbf{R}'_4 = \mathcal{A}_{43} \cdot \mathbf{X}'_4$. Finally, \mathbf{R}''_4 is restored using the position coordinates \mathcal{L}_p , transitioning $\mathbf{R}'_4 \in \mathbb{R}^{\frac{H}{2} \times \frac{W}{2} \times \frac{C}{4}} \xrightarrow{\mathcal{L}_p} \mathbf{R}''_4 \in \mathbb{R}^{H \times W \times \frac{C}{4}}$, and $\mathbf{R}_4 = BN(\mathbf{R}''_4 + \mathbf{X}_4)$.

For stage 4, we once again employ the widely used vision attention mechanism with the head_num=4, denoted as \mathcal{A}_{44} , applied to \mathbf{X}_4 . This yields the feature \mathbf{R}_4 , which $\mathbf{R}_4 = BN(\mathcal{A}_{44} \cdot \mathbf{X}_4 + \mathbf{X}_4)$.

Subsequently, the features $\{\mathbf{R}_1, \mathbf{R}_2, \mathbf{R}_3, \mathbf{R}_4\}$ are concatenated together to produce the out feature \mathbf{Y} .

IV. EXPERIMENTS

This section presented a comprehensive analysis of LWGANet’s experimental performance across twelve datasets encompassing RS scene classification, object detection, semantic segmentation, and change detection tasks. Consistent with established methodologies in the domain [42], [43], our experiments on detection, segmentation, and change detection tasks utilized a backbone pre-trained for 300 epochs on the ImageNet-1K [44] dataset.

A. RS Scene Classification

1) *Datasets*: LWGANet was evaluated on three widely recognized RS scene classification datasets for the experiments: UCM [24], AID [25], and NWPU [26]. The UCM dataset consisted of 2,100 images distributed across 21 categories, with each category containing 100 images of 256×256 pixels. The AID dataset encompassed 10,000 images across 30 categories, all sized at 600×600 pixels. The NWPU dataset included

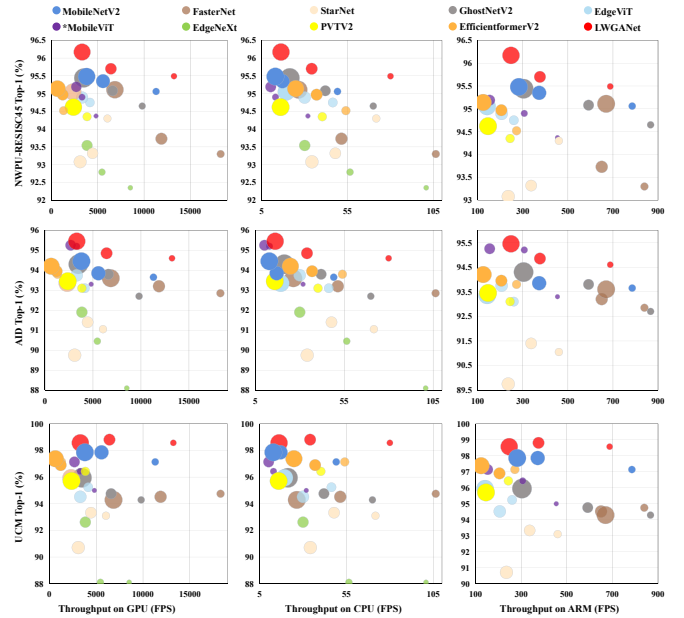


Fig. 5: Comprehensive comparison of top-1 accuracy, FPS, and parameters on the NWPU, AID, and UCM datasets. The area of each circle was proportional to the number of parameters in model. LWGANet with red circles achieved the best balance.

31,500 images across 45 categories, with each category comprising 700 images of 256×256 pixels. These datasets were divided into training and validation sets in an 8:2 ratio. Models were trained from scratch for 300 epochs without the use of pre-trained weights to assess their inherent fitting capabilities.

2) *Experimental Setup*: The training and validation image size was set to 224×224 pixels. A fixed seed of 1234 was used for all operations to ensure consistency. The AdamW [55] optimizer was utilized for optimizing the model. The learning rate was set to 0.0001 with a weight decay of 0.05. The batch size for the experiments was 64, and a cosine decay schedule was applied for adjusting the learning rate. A warm up phase was included for the initial 2 epochs with a factor of 0.001. Data augmentation techniques such as random resized cropping, random horizontal flipping, and random augment [56] were employed in the training process. The loss function used in the experiments was cross-entropy loss. This configuration ensured a robust setup for evaluating the classification capabilities of LWGANet under controlled and consistent conditions.

3) *Experimental Results*: Table II displayed the performance comparison of LWGANet against several different types of state-of-the-art (SOTA) lightweight models on these classification datasets. We presented results for backbone type, parameters (Params.), floating point operations (FLOPs), top-1 accuracy (Acc.), and throughput (frames per second, FPS) across different methods. Throughput was acquired through execution on both the NVIDIA GeForce RTX 3090 (GPU), Intel i9-11900K (CPU), and NVIDIA AGX-XAVIER (ARM) platforms. LWGANet consistently outperformed the selected SOTA models across all datasets. For example, on the NWPU dataset, LWGANet L0 achieved a top-1 accuracy of 95.49%,

TABLE II: Experimental results on NWPU [26], AID [25], and UCM [24] classification datasets. The symbol ‘*’ indicated a training image size of 256×256. FPS were acquired through execution on both the NVIDIA GeForce RTX 3090 (GPU), Intel i9-11900K (CPU), and NVIDIA AGX-XAVIER (ARM) platforms with batch sizes of 256, 16, and 32, respectively.

Model	Publication Year	Backbone Type	Params. (M) ↓	FLOPs (G) ↓	Top-1 Accuracy (%) ↑			Throughput (FPS) ↑		
					NWPU [26]	AID [25]	UCM [24]	GPU	CPU	ARM
MobileNet V2 1.0× [28]	CVPR 2018	CNN	2.28	0.319	95.06	93.65	97.14	11301	49.11	785.4
FasterNet T0 [10]	CVPR 2023	CNN	2.68	0.338	93.30	92.85	94.75	18276	106.4	839.7
StarNet S1 [37]	CVPR 2024	CNN	2.68	0.431	94.30	91.05	93.10	6045	71.70	459.8
EdgeViT XXS [38]	ECCV 2022	Transformer	3.79	0.546	94.75	93.10	95.24	4153	46.36	259.9
EfficientformerV2 S0 [9]	ICCV 2023	Transformer	3.36	0.396	94.52	93.80	97.14	1299	54.00	272.0
EdgeNeXt XXS [39]	ECCVW 2022	Hybrid	1.17	0.197	92.35	88.10	88.10	8521	100.8	-
*MobileViT XXS [40]	ICLR 2022	Hybrid	1.03	0.333	94.37	93.30	95.00	4811	31.87	453.6
GhostNet V2 0.6× [12]	NeurIPS 2022	Hybrid	2.16	0.077	94.65	92.70	94.29	9802	69.96	867.1
LWGANet L0	-	Hybrid	1.72	0.186	95.49	94.60	98.57	13234	80.00	687.8
MobileNet V2 2.0× [28]	CVPR 2018	CNN	8.81	1.17	95.35	93.85	97.86	5567	17.03	372.3
FasterNet T1 [10]	CVPR 2023	CNN	6.37	0.855	93.73	93.20	94.52	11876	51.42	650.1
StarNet S3 [37]	CVPR 2024	CNN	5.5	0.767	93.32	91.40	93.33	4438	47.86	336.8
EdgeViT XS [38]	ECCV 2022	Transformer	6.40	1.12	94.89	93.75	94.52	3310	29.95	205.8
PVT V2 B0 [41]	CVM 2022	Transformer	3.42	0.533	94.35	93.10	96.43	3843	40.26	243.4
EfficientformerV2 S1 [9]	ICCV 2023	Transformer	5.87	0.661	94.97	93.95	96.90	1211	36.96	204.5
EdgeNeXt XS [39]	ECCVW 2022	Hybrid	2.15	0.408	92.79	90.45	88.10	5455	56.42	-
*MobileViT XS [40]	ICLR 2022	Hybrid	2.02	0.900	94.90	95.20	96.43	3300	12.99	306.3
GhostNet V2 1.0× [12]	NeurIPS 2022	Hybrid	4.93	0.181	95.08	93.80	94.76	6596	42.02	591.7
LWGANet L1	-	Hybrid	5.90	0.709	95.70	94.85	98.81	6418	34.08	375.8
MobileNet V2 2.5× [28]	CVPR 2018	CNN	13.7	1.80	95.48	94.45	97.86	3796	12.90	282.4
FasterNet T2 [10]	CVPR 2023	CNN	13.8	1.91	95.11	93.60	94.29	6852	26.40	669.8
StarNet S4 [37]	CVPR 2024	CNN	7.23	1.07	93.08	89.75	90.71	3093	34.20	235.1
EdgeViT S [38]	ECCV 2022	Transformer	12.7	1.90	95.05	93.35	95.95	2318	19.31	141.3
PVT V2 B1 [41]	CVM 2022	Transformer	13.5	2.04	94.62	93.45	95.71	2369	15.96	145.3
EfficientformerV2 S2 [9]	ICCV 2023	Transformer	12.3	1.26	95.14	94.20	97.38	642	24.74	123.8
EdgeNeXt S [39]	ECCVW 2022	Hybrid	5.30	0.960	93.54	91.90	92.62	3844	30.00	-
*MobileViT S [40]	ICLR 2022	Hybrid	5.03	1.75	95.19	95.25	97.14	2681	10.20	152.7
GhostNet V2 2.0× [12]	NeurIPS 2022	Hybrid	16.7	0.632	95.44	94.30	95.95	3476	21.32	303.2
LWGANet L2	-	Hybrid	13.0	1.87	96.17	95.45	98.57	3308	16.18	274.3

TABLE III: Experimental results on DOTA 1.0 test set [45] compared with SOTA methods with single-scale training and testing. Red and blue denoted the best and second-best performance of each column. *E-FormerV2-S2 denoted EfficientFormerV2 S2.

Methods	Backbone	Params. (M) ↓	FLOPs (G) ↓	mAP (%) ↑	AP per category (%) ↑															
					PL	BD	BR	GTF	SV	LV	SH	TC	BC	ST	SBF	RA	HA	SP	HC	
RoI Trans. [46]	ResNet-50 [33]	55.1	225.3	74.05	89.01	77.48	51.64	72.07	74.43	77.55	87.76	90.81	79.71	85.27	58.36	64.11	76.50	71.99	54.06	
G.V. [47]	ResNet-50 [33]	41.1	211.3	75.02	89.64	85.00	52.26	77.34	73.01	73.14	86.82	90.74	79.02	86.81	59.55	70.91	72.94	70.86	57.32	
DCFL [48]	ResNet-50 [33]	36.1	157.8	75.35	-	-	-	-	-	-	-	-	-	-	-	-	-	-	-	
AOPG [49]	ResNet-101 [33]	-	-	75.39	89.14	82.74	51.87	69.28	77.65	82.42	88.08	90.89	86.26	85.13	60.60	66.30	74.05	67.76	58.77	
ReDet [50]	ReResNet [50]	-	-	76.25	88.79	82.64	53.97	74.00	78.13	84.06	88.04	90.89	87.78	85.75	61.76	60.39	75.96	68.07	63.59	
Oriented R-CNN [51]	ResNet-50 [33]	41.1	211.4	75.87	89.46	82.12	54.78	70.86	78.93	83.00	88.20	90.90	87.50	84.68	63.97	67.69	74.94	68.84	52.28	
	FasterNet-T2 [10]	30.0	160.3	76.17	89.51	78.20	52.65	73.11	78.36	83.39	87.80	90.86	87.58	84.60	62.22	61.89	75.04	71.03	66.28	
	*E-FormerV2-S2 [9]	29.2	145.1	76.70	89.55	84.12	53.39	74.40	80.70	84.84	87.92	90.89	87.44	84.47	60.88	67.43	77.63	67.62	59.16	
	ARC-R50 [52]	74.4	212.0	77.35	89.40	82.48	55.33	73.88	79.37	84.05	88.06	90.90	86.44	84.83	63.63	70.32	74.29	71.91	65.43	
	Swin-T-RSP [53]	44.8	215.7	76.07	89.48	82.23	52.25	74.37	77.99	83.55	88.02	90.90	87.42	84.92	57.70	65.99	73.88	69.30	63.07	
	LSKNet-S [42]	31.0	161.0	77.49	89.66	85.52	57.72	75.70	74.95	78.69	88.24	90.88	86.79	86.38	66.92	63.77	77.77	74.47	64.82	
	DecoupleNet-D2 [54]	23.3	142.4	78.04	89.37	83.25	54.29	75.51	79.83	84.82	88.49	90.89	87.19	86.23	66.07	65.53	77.23	72.34	69.62	
	PKINet-S [43]	30.8	184.6	78.39	89.72	84.20	55.81	77.63	80.25	84.45	88.12	90.88	87.57	86.07	66.86	70.23	77.47	73.62	62.94	
	LWGANet-L2	29.2	159.1	78.64	89.68	82.82	55.17	77.48	80.13	84.93	88.22	90.90	87.82	85.64	65.48	67.49	77.10	73.12	73.57	

significantly surpassing StarNet S1’s accuracy of 94.30%, while maintaining faster inference speeds (13,234 versus 6,045 FPS on the GPU device) and using fewer parameters and FLOPs (1.72M and 0.186G versus 2.68M and 0.431G).

4) *Practical Inference Speed*: In considering the practical deployment of models on resource-constrained devices, we measured the inference FPS of LWGANet and other models on the GPU, CPU, and ARM. As indicated in Fig. 5, LWGANet offered an optimal balance between accuracy, parameters, and FPS across GPU, ARM, and CPU devices on the UCM, AID, and NWPU datasets.

B. RS Object Detection

1) *Detection Datasets*: For RS object detection, LWGANet was assessed on three established oriented object detection datasets: DOTA 1.0 [45], DOTA 1.5 [45], and DIOR-R [49]. DOTA 1.0 includes 2,806 RS images, divided into 1,411 for training, 458 for validation, and 937 for testing, with a total of 188,282 instances across 15 categories. DOTA 1.5, an enhancement of DOTA 1.0, introduced an additional category—container crane—and a significant increase in instances smaller than 10 pixels, bringing the total to 403,318 instances.

TABLE IV: Experimental results on DIOR-R test set [49] compared with SOTA methods. Complexities were tested by 800×800.

Methods	G.V. [47]	RoI Trans. [46]	AOPG [49]	LSKNet-S [42]	Oriented Rep [57]	PKINet-S [43]	DecoupleNet-D2 [54]	LWGANet-L2
Params. ↓	41.1	55.1	-	31.0	36.6	30.8	23.3	29.2
FLOPs ↓	134.4	148.4	-	173.6	118.8	118.1	92.4	102.7
mAP ↑	60.06	63.87	64.41	65.90	66.71	67.03	67.08	68.53

TABLE V: Experimental results on DOTA 1.5 test set [45] compared with SOTA methods with single-scale training and testing.

Methods	RoI Trans. [46]	ReDet [50]	DCFL-R50 [48]	LSKNet-S [42]	PKINet-S [43]	LWGANet-L2
mAP ↑	65.03	66.86	67.37	70.24	71.47	71.72

TABLE VI: Comparison with different backbones on DOTA 1.0 test set [45]. All the backbones were built within O-RCNN [51] decoder. Complexities were computed for backbones only. Speeds were tested on the RTX 3090 GPU.

Methods	ARC-R50 [52]	LSKNet-S [42]	PKINet-S [43]	LWGANet-L2
Params. ↓	56.5M	14.4M	13.7M	12.0M
FLOPs ↓	86.6G	54.4G	70.2G	38.8G
FPS ↑	11.8	22.5	5.4	19.4
mAP ↑	77.35	77.49	78.39	78.64

DIOR-R featured oriented bounding box annotations based on the DIOR dataset [58], with 11,725 images for training, 11,738 for testing, and 192,518 annotations, each image sized at 800×800 pixels. Data preprocessing and training protocols aligned with established methods [59], [43] across the datasets. In detection experiments, Oriented R-CNN (O-RCNN) [51] was utilized as the decoder for LWGANet.

2) *Experimental Results:* Tables III, IV, and V detailed the performance of LWGANet compared to various methods on the DOTA 1.0, DIOR-R, and DOTA 1.5 datasets, respectively. We computed the mean average precision (mAP) on the test sets following single-scale training and testing protocols. Across all three datasets, LWGANet consistently outperformed competing models while using fewer parameters. For instance, on the DOTA 1.0 test set, LWGANet L2 recorded a mAP of 78.64% with a minimal parameter count of 29.2M, surpassing the SOTA models. Similarly, on the DIOR-R test set, LWGANet L2 achieved a mAP of 68.53%, which was 1.5% higher than that of PKINet [43], with reduced parameters and FLOPs. Comparable outcomes were observed on the DOTA 1.5 test set. These findings underscored LWGANet’s robustness and efficacy in RS oriented object detection.

Additionally, Table VI contrasted LWGANet with various backbone networks specifically designed for RS object detection in terms of parameters, FLOPs, and inference FPS. LWGANet demonstrated superior mAP, lower parameter usage, 60% fewer FLOPs, and higher FPS compared to PKINet. Notably, with the same decoder, LWGANet excelled over other specialized RS object detection backbones in mAP, parameters, and FLOPs, underscoring its efficiency and effectiveness.

3) *Visualization results:* The results from the DOTA1.0 test dataset were depicted in Fig. 6. The visual analysis selectively utilized the SOTA backbones, ARC-R50 [52] and PKINet [43], which were specifically engineered for RS object detection, alongside the inclusion of contemporary conventional lightweight backbones such as FasterNet [10] and EfficientFormerV2 [9]. As illustrated in Fig. 6, the vi-



Fig. 6: Visual results on DOTA 1.0 test sets. Oriented R-CNN [51] was used as the detection head.

ual results revealed that LWGANet proficiently discriminated between diverse objects, effectively handling significant scale variations observed in objects such as harbors, diminutive ships, and larger vessels. Conversely, conventional lightweight backbones [10], [9] exhibited sub-optimal performance when confronted with the complexities presented by multi-scale images within a single frame, as discussed upon in both the abstract and introduction sections of this article.

C. RS Semantic Segmentation

1) *Segmentation Datasets:* LWGANet was evaluated on two prominent RS semantic segmentation datasets for our experiments: UAVid [1] and LoveDA [67]. Both datasets employed online testing protocols for their test sets. The UAVid dataset, a high-resolution unmanned aerial vehicle (UAV) semantic segmentation dataset, focused on urban street scenes and offered two spatial resolutions (3840×2160 and 4096×2160) across eight classes. It contained 42 sequences totaling 420 images, distributed as 200 for training, 70 for validation, and 150 for testing. The LoveDA dataset featured 5,987 fine-resolution optical RS images (GSD 0.3 m) each sized at 1024×1024 pixels, spanning seven landcover categories. This dataset included 2,522 training images, 1,669 validation images, and 1,796 testing images. Data preprocessing and training protocols were adopted from UnetFormer [2], which

TABLE VII: Segmentation experimental results on UAVid test set [1] with lightweight SOTA. Complexities and speeds were tested by 1024×1024 input on the RTX 3090 GPU.

Methods	Backbone	Params. (M) ↓	FLOPs (G) ↓	Speed (FPS) ↓	mIoU (%) ↑	IoU per category (%) ↑							
						Clutter	Building	Road	Tree	Vegetation	Moving Car	Static Car	Human
SwiftNet [60]	ResNet18 [33]	11.8	51.6	138.7	61.1	64.1	85.3	61.5	78.3	76.4	51.1	62.1	15.7
BiSeNet [61]	ResNet18 [33]	12.9	51.8	121.9	61.5	64.7	85.7	61.1	78.3	77.3	48.6	63.4	17.5
MANet [62]	ResNet18 [33]	12.0	51.7	75.6	62.6	64.5	85.4	77.8	77.0	60.3	67.2	53.6	14.9
BoTNet [63]	ResNet18 [33]	17.6	49.9	135.0	63.2	64.5	84.9	78.6	77.4	60.5	65.8	51.9	22.4
ABCNet [64]	ResNet18 [33]	14.0	62.9	102.2	63.8	67.4	86.4	81.2	79.9	63.1	69.8	48.4	13.9
CoaT [65]	CoaT-Mini [65]	11.1	104.8	10.6	65.8	69.0	88.5	80.0	79.3	62.0	70.0	59.1	18.9
SegFormer [66]	MIT-B1 [66]	13.7	63.3	31.3	66.0	66.6	86.3	80.1	79.6	62.3	72.5	52.5	28.5
UnetFormer [2]	EfficientFormerV2-S2 [9]	12.7	35.8	54.1	65.2	63.8	82.5	78.9	78.0	63.0	73.5	51.7	29.9
	FasterNet-T2 [10]	13.3	49.1	198.8	65.7	65.3	86.2	79.6	78.8	62.1	70.9	54.8	28.1
	DecoupleNet-D2 [54]	6.8	32.1	-	65.8	65.1	85.4	80.6	78.8	62.1	74.1	49.7	30.8
	ResNet18 [33]	11.7	46.9	115.6	67.8	68.4	87.4	81.5	80.2	63.5	73.6	56.4	31.0
	LWGANet-L2	12.6	50.3	67.3	69.1	69.0	87.9	81.9	80.5	64.6	76.7	59.7	32.7

TABLE VIII: Segmentation experimental results on LoveDA test set [67] with SOTA models.

Decoder	Backbone	Publication	mIoU ↑
FarSeg [68]	ResNet50 [33]	CVPR 2020	50.1
Segmenter [69]	ViT-Tiny [18]	ICCV 2021	47.1
SegFormer [66]	MIT-B5 [66]	NeurIPS 2021	47.5
UperNet [70]	Swin-Tiny [20]	ICCV 2021	50.0
FactSeg [71]	ResNet50 [33]	TGRS 2021	50.0
UnetFormer [2]	ResNet18 [33]	ISPRS 2022	52.4
RSSFormer [72]	RSS-B [72]	TIP 2023	52.4
LoveNAS [73]	ResNet50 [33]	ISPRS 2024	52.3
UnetFormer [2]	LWGANet-L2	-	53.6

UnetFormer also served as the decoder for LWGANet in these segmentation experiments.

2) *Experimental Results:* Tables VII and VIII detailed the performance comparisons of LWGANet against various models on the UAVid and LoveDA datasets, respectively, with evaluations based on mean intersection over union (mIoU) on the test sets. LWGANet consistently delivered superior performance on both datasets. Notably, on the UAVid test set, LWGANet L2 achieved SOTA results with a total parameter count of 12.6M, surpassing UNetFormer by 1.3% in mIoU. Similarly, on the LoveDA test set, LWGANet L2 recorded an mIoU of 53.6%, exceeding both UNetFormer and RSSFormer by 1.2%. These findings highlighted LWGANet’s exceptional performance and versatility in addressing RS semantic segmentation challenges.

3) *Visualization results:* As shown in Fig. 7. The LoveDA segmentation visualization results demonstrated the unique advantage of LWGANet in handling detailed features such as roads and buildings due to the presence of the LWGA module.

D. RS Change Detection

1) *Change Detection Datasets:* LWGANet was evaluated in RS change detection across four established datasets: LEVIR-CD [74], WHU-CD [75], CDD-CD [76], and SYSU-CD [77]. Each dataset adhered to the standard split into training, validation, and test sets, with the best validation weights applied for testing. Consistent with prior research [84], [85], data preprocessing and training schedules were maintained for uniformity. For the change detection experiments, LWGANet utilized A2Net [84] and CLAFa [85] as the decoders.

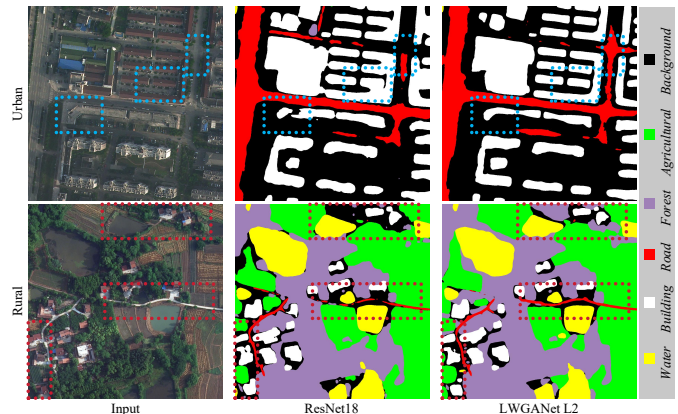


Fig. 7: Visual results on LoveDA test set. UnetFormer was used as segmentation head.

2) *Experimental Results:* Table IX illustrated the performance comparison of LWGANet against various models on the LEVIR-CD, WHU-CD, CDD-CD, and SYSU-CD datasets. Evaluation metrics included IoU, F1 score, and precision of changed regions on the respective test sets. LWGANet consistently outperformed other models across all four datasets while maintaining similar parameters. For example, LWGANet L2 with a CLAFa decoder achieved SOTA results on the LEVIR-CD test set, with a total parameter count of 16.1M. On the WHU-CD test set, LWGANet L2 with a CLAFa decoder achieved an IoU of 90.92%, surpassing CLAFa-ResNet18 by 1.18%. Similar performance enhancements were observed on the CDD-CD and SYSU-CD test sets. These findings underscored LWGANet’s remarkable performance and adaptability in RS change detection tasks.

E. Ablation Studies

A series of ablation experiments were initially conducted on the GPA, RLA, SMA, and SGA modules in the context of the RS object detection task, employing the DOTA1.0 dataset for both training and validation. The results of these ablation experiments were presented in Table X. The first four rows represented different methods, where all features were extracted through a single module with different channels for similar number of parameters and FLOPs, thus assessing the impact of individual modules on various types of objects.

TABLE IX: Change detection experimental results on LEVIR-CD test set [74], WHU-CD test set [75], CDD-CD test set [76], and SYSU-CD test set [77] with SOTA models.

Methods	Params. (M) ↓	FLOPs (B) ↓	LEVIR-CD [74]			WHU-CD [75]			CDD-CD [76]			SYSU-CD [77]		
			IoU ↑	F1 ↑	Pre ↑	IoU ↑	F1 ↑	Pre ↑	IoU ↑	F1 ↑	Pre ↑	IoU ↑	F1 ↑	Pre ↑
IFNet [78]	35.7	82.3	80.36	89.11	91.64	73.16	84.50	87.92	85.68	92.29	92.03	64.42	78.36	78.49
BIT [79]	3.50	10.6	81.30	89.69	92.33	78.24	87.79	85.07	70.22	82.50	89.03	60.48	75.38	80.08
ChangeFormer [80]	41.0	203	81.59	89.86	91.12	72.92	84.34	89.08	85.40	92.13	93.39	64.20	78.20	79.70
ICIFNet [81]	23.8	25.4	81.75	89.96	91.32	79.24	88.32	92.98	85.73	92.31	93.41	40.65	57.80	71.35
DMINet [82]	6.24	14.6	82.99	90.75	92.52	79.68	88.69	93.84	86.91	92.99	93.03	51.56	68.04	64.47
CSViG [83]	38.0	203	84.37	91.52	92.35	82.76	90.57	94.69	87.60	93.39	94.48	69.21	81.80	84.43
A2Net-MobileNetv2 [84]	3.78	3.05	84.14	91.39	91.50	88.98	94.14	97.04	87.39	93.27	93.43	71.06	83.08	85.48
CLAFA-MobileNetv2 [85]	5.06	16.6	84.87	91.82	91.85	88.76	94.05	95.38	87.56	93.37	92.78	69.72	82.16	85.15
CLAFA-ResNet18 [85]	14.7	22.0	85.21	92.01	92.96	89.74	94.59	95.59	88.19	93.73	91.87	70.12	82.43	83.66
A2Net-LWGANet L0	2.91	2.76	84.31	91.49	92.94	88.68	94.00	95.95	87.38	93.27	94.45	70.68	82.82	85.49
CLAFA-LWGANet L0	4.18	16.4	84.96	91.87	93.13	89.39	94.40	96.21	87.94	93.58	92.28	69.33	81.89	85.11
A2Net-LWGANet L2	14.3	7.72	84.90	91.83	92.79	90.22	94.86	96.88	87.80	93.50	94.09	71.98	83.70	86.54
CLAFA-LWGANet L2	16.1	22.1	85.90	92.42	93.25	90.92	95.24	96.51	88.27	93.77	91.76	70.79	82.90	87.69

TABLE X: Ablation experimental results on DOTA 1.0 val set [45] with single-scale training and testing. All the backbones were pre-trained on Imagenet1k for 100 epochs, and the decoder was trained on the DOTA1.0 train set with the O-RCNN [51] decoder for 30 epochs. GPA, RLA, SMA, SGA, and LWGANet had stem dims of 64, 64, 96, 96, and 96, respectively.

Methods	Params.	FLOPs	mAP	PL	BD	BR	GTF	SV	LV	SH	TC	BC	ST	SBF	RA	HA	SP	HC
GPA	28.1	157.0	68.4	89.1	73.9	46.9	70.7	62.1	82.2	88.8	90.6	71.8	60.8	63.3	61.8	67.1	54.8	42.4
RLA	29.0	159.9	70.3	89.8	75.7	49.2	75.9	65.2	84.3	89.0	90.7	76.5	62.3	64.8	65.6	75.2	55.1	34.4
SMA	27.1	152.0	70.5	89.7	77.1	47.5	78.2	64.5	85.2	89.1	90.7	68.1	62.2	64.3	65.1	76.4	50.1	49.1
SGA	34.3	161.7	71.0	89.6	77.0	48.8	73.4	59.0	85.2	89.0	90.6	72.3	61.6	66.1	66.7	74.8	57.7	52.8
LWGANet-L2	29.2	159.1	74.1	90.0	79.7	57.8	79.8	69.4	85.4	89.6	90.7	74.1	62.1	70.1	67.3	76.2	60.1	59.2

TABLE XI: Ablation experimental results on the NWPU val set [26], DOTA 1.0 val set [45], UAVid test set [1], and LEVIR-CD test set [74]. The first line represented feature extraction through the RLA single module. The O-RCNN [51], UnetFormer [2], and A2Net [84] were used for the decoder on detection, segmentation, and change detection tasks, respectively.

GPA	RLA	SMA	SGA	Classification				Detection		Segmentation		Change detection	
				Params.	FLOPs	Acc. (%) ↑	FPS ↑	Params. ↓	mAP (%) ↑	Params. ↓	mIoU (%) ↑	Params. ↓	IoU (%) ↑
				27.69	4.35	95.35	3819	43.9	69.64	27.2	62.03	28.96	83.66
✓	✓	✓		12.54	1.84	95.83	3983	28.6	70.56	12.1	62.16	13.80	83.23
✓	✓		✓	12.90	1.87	95.51	3942	29.1	71.10	12.4	61.82	14.17	83.73
✓		✓	✓	11.95	1.70	95.86	3490	28.2	70.09	11.5	61.71	13.21	83.50
	✓	✓	✓	12.06	1.71	95.98	3638	28.3	71.16	11.6	61.90	13.33	83.74
✓	✓	✓	✓	13.01	1.87	96.17	3308	29.2	71.59	12.6	62.05	14.30	83.95

From Table X, it was apparent that the standalone utilization of the GPA module yielded relatively weaker feature extraction capability, resulting in overall poorer performance.

The RLA module demonstrated reasonable feature extraction capability, performing well on small objects like small vehicles (SV) and swimming pools (SP). Specially, due to the inherent characteristics of standard convolution, the RLA module possessed a natural advantage in extracting features from regular-shaped objects, such as bridges (BR) and basketball courts (BC), but its performance was less satisfactory on irregular objects like helicopters (HC).

The standalone SMA module primarily excelled in capturing features from larger and irregular objects, such as baseball diamonds (BD), ground track fields (GTF), harbors (HA), and HC. Similarly, the standalone SGA module’s feature extraction advantage was more pronounced for irregular large objects like roundabouts (RA) and soccer ball fields (SBF), irregular objects like HC. The results for the SV objects showed that GPA and RLA exhibited relatively robust feature extraction capabilities, while SMA and SGA performed less effectively.

The last row showcased the results for LWGANet L2. It was evident that, with the incorporation of group attention, the overall performance of the objects improved. Notably, some objects even achieved higher AP compared to the performance of individual modules. This further underscored the advantage of the LWGA module in simultaneously capturing details and overall features.

In Table XI, we presented the ablation study results for LWGANet across four tasks. The first row represented the configuration where all features were extracted through the RLA module with 96 channels. To enhance experimental efficiency, the models in this ablation study were trained without pre-trained weights. The results demonstrated that, with the exception of a negative impact from global attention on semantic segmentation tasks, all modules exhibited positive enhancements in the other tasks, thereby validating the effectiveness of LWGANet in RS visual tasks.

The class activation mapping (CAM) heatmaps from the ablation experiments in Fig. 8 revealed that LWGANet prioritized different objects at various stages, during the processing

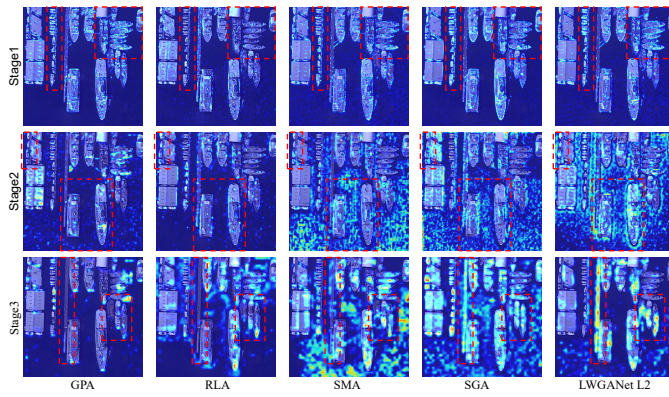


Fig. 8: The CAM visual results of different methods. All backbones were pre-training for 100 epoch on Imagenet1k, and training decoder for 30 epoch on DOTA1.0 train set with O-RCNN decoder. The figure selected from its test set.

of multi-scale objects, thereby significantly outperforming models comprised of a single module.

F. Limitations and Future Works

The determination of an optimal attention distance for SMA in our experiments should have been approached with caution, as its effectiveness might have varied across different datasets due to the diverse characteristics of objects. Future endeavors will delve into exploring attention distances and their geometrical configurations to deepen our understanding of their impact on various visual tasks. Furthermore, while LWGANet surpassed SOTA methods with fewer parameters and FLOPs in RS object detection and semantic segmentation tasks, its performance in terms of FPS required further investigation. Addressing the underperformance in FPS was a key focus of the ongoing research, aimed at identifying and remedying the underlying causes of this phenomenon.

V. CONCLUSION

This study introduces LWGANet, a novel lightweight backbone network tailored for RS visual tasks. LWGANet incorporates the LWGA module to enhance feature representation and robustness for multi-scale targets, effectively addressing the challenge encountered by existing lightweight networks in extracting features from multi-scale objects in RS images. Extensive experiments were conducted across 12 datasets, encompassing four tasks: RS scene classification, object detection, semantic segmentation, and change detection. The experimental findings showcase LWGANet’s superiority over existing SOTA methods in terms of both accuracy and lightweight efficiency. Additionally, LWGANet offers a fresh solution for RS visual tasks on resource-constrained devices and LWGA module provides valuable insights for the advancement of lightweight networks.

REFERENCES

[1] Y. Lyu, G. Vosselman, G.-S. Xia, A. Yilmaz, and M. Y. Yang, “Uavid: A semantic segmentation dataset for uav imagery,” *ISPRS J. Photogramm. Remote Sens.*, vol. 165, pp. 108–119, 2020.

[2] L. Wang, R. Li, C. Zhang, S. Fang, C. Duan, X. Meng, and P. M. Atkinson, “Unetformer: A unet-like transformer for efficient semantic segmentation of remote sensing urban scene imagery,” *ISPRS J. Photogramm. Remote Sens.*, vol. 190, pp. 196–214, 2022.

[3] T.-Y. Lin, P. Dollár, R. Girshick, K. He, B. Hariharan, and S. Belongie, “Feature pyramid networks for object detection,” in *IEEE Comput. Vis. Pattern Recog.*, 2017, pp. 2117–2125.

[4] M. Tan, R. Pang, and Q. V. Le, “Efficientdet: Scalable and efficient object detection,” in *IEEE Comput. Vis. Pattern Recog.*, 2020, pp. 10781–10790.

[5] S. Qiao, L.-C. Chen, and A. Yuille, “Detectors: Detecting objects with recursive feature pyramid and switchable atrous convolution,” in *IEEE Comput. Vis. Pattern Recog.*, 2021, pp. 10213–10224.

[6] J. Feng, X. Wu, R. Shang, C. Sui, J. Li, L. Jiao, and X. Zhang, “Attention multibranch convolutional neural network for hyperspectral image classification based on adaptive region search,” *IEEE Trans. Geosci. Remote Sens.*, vol. 59, no. 6, pp. 5054–5070, 2021.

[7] S.-B. Chen, Q.-S. Wei, W.-Z. Wang, J. Tang, B. Luo, and Z.-Y. Wang, “Remote sensing scene classification via multi-branch local attention network,” *IEEE Trans. Image Proc.*, vol. 31, pp. 99–109, 2022.

[8] J. Yang, B. Du, Y. Xu, and L. Zhang, “Can spectral information work while extracting spatial distribution?—an online spectral information compensation network for hsi classification,” *IEEE Trans. Image Proc.*, vol. 32, pp. 2360–2373, 2023.

[9] Y. Li, J. Hu, Y. Wen, G. Evangelidis, K. Salahi, Y. Wang, S. Tulyakov, and J. Ren, “Rethinking vision transformers for mobilenet size and speed,” in *IEEE Int. Conf. Comput. Vis.*, 2023, pp. 16889–16900.

[10] J. Chen, S.-h. Kao, H. He, W. Zhuo, S. Wen, C.-H. Lee, and S.-H. G. Chan, “Run, don’t walk: Chasing higher flops for faster neural networks,” in *IEEE Comput. Vis. Pattern Recog.*, 2023, pp. 12021–12031.

[11] K. Han, Y. Wang, Q. Tian, J. Guo, C. Xu, and C. Xu, “Ghostnet: More features from cheap operations,” in *IEEE Comput. Vis. Pattern Recog.*, 2020, pp. 1580–1589.

[12] Y. Tang, K. Han, J. Guo, C. Xu, C. Xu, and Y. Wang, “Ghostnetv2: Enhance cheap operation with long-range attention,” in *Neur. Inf. Proc. Syst.*, vol. 35, 2022, pp. 9969–9982.

[13] A. Krizhevsky, I. Sutskever, and G. E. Hinton, “Imagenet classification with deep convolutional neural networks,” in *Neur. Inf. Proc. Syst.*, 2012, pp. 1106–1114.

[14] A. G. Howard, M. Zhu, B. Chen, D. Kalenichenko, W. Wang, T. Weyand, M. Andreetto, and H. Adam, “Mobilenets: Efficient convolutional neural networks for mobile vision applications,” *arXiv preprint arXiv:1704.04861*, 2017.

[15] Y.-J. Zheng, S.-B. Chen, C. H. Ding, and B. Luo, “Model compression based on differentiable network channel pruning,” *IEEE Trans. Neural Networks Learn. Syst.*, vol. 34, no. 12, pp. 10203–10212, 2023.

[16] X. Ding, X. Zhang, N. Ma, J. Han, G. Ding, and J. Sun, “Repvgg: Making vgg-style convnets great again,” in *IEEE Comput. Vis. Pattern Recog.*, 2021, pp. 13733–13742.

[17] X. Dong and Y. Yang, “Network pruning via transformable architecture search,” in *Neur. Inf. Proc. Syst.*, vol. 32, 2019.

[18] A. Dosovitskiy, L. Beyer, A. Kolesnikov, D. Weissenborn, X. Zhai, T. Unterthiner, M. Dehghani, M. Minderer, G. Heigold, S. Gelly, J. Uszkoreit, and N. Houlsby, “An image is worth 16x16 words: Transformers for image recognition at scale,” *ArXiv*, vol. abs/2010.11929, 2020.

[19] W. Wang, E. Xie, X. Li, D.-P. Fan, K. Song, D. Liang, T. Lu, P. Luo, and L. Shao, “Pyramid vision transformer: A versatile backbone for dense prediction without convolutions,” in *IEEE Int. Conf. Comput. Vis.*, 2021, pp. 568–578.

[20] Z. Liu, Y. Lin, Y. Cao, H. Hu, Y. Wei, Z. Zhang, S. Lin, and B. Guo, “Swin transformer: Hierarchical vision transformer using shifted windows,” in *IEEE Int. Conf. Comput. Vis.*, 2021, pp. 9992–10002.

[21] Y. Li, G. Yuan, Y. Wen, J. Hu, G. Evangelidis, S. Tulyakov, Y. Wang, and J. Ren, “Efficientformer: Vision transformers at mobilenet speed,” in *Neur. Inf. Proc. Syst.*, vol. 35, 2022, pp. 12934–12949.

[22] I. O. Tolstikhin, N. Houlsby, A. Kolesnikov, L. Beyer, X. Zhai, T. Unterthiner, J. Yung, A. Steiner, D. Keysers, J. Uszkoreit *et al.*, “Mlp-mixer: An all-mlp architecture for vision,” in *Neur. Inf. Proc. Syst.*, vol. 34, 2021, pp. 24261–24272.

[23] K. Han, Y. Wang, J. Guo, Y. Tang, and E. Wu, “Vision GNN: An image is worth graph of nodes,” in *Neur. Inf. Proc. Syst.*, vol. 35, 2022, pp. 8291–8303.

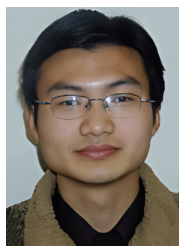
[24] Y. Yang and S. Newsam, “Bag-of-visual-words and spatial extensions for land-use classification,” in *Proc. 18th SIGSPATIAL Int. Symp. on Adv. in Geogr. Inf. Syst.*, 2010, pp. 270–279.

- [25] G.-S. Xia, J. Hu, F. Hu, B. Shi, X. Bai, Y. Zhong, L. Zhang, and X. Lu, "Aid: A benchmark data set for performance evaluation of aerial scene classification," *IEEE Trans. Geosci. Remote Sens.*, vol. 55, no. 7, pp. 3965–3981, 2017.
- [26] G. Cheng, J. Han, and X. Lu, "Remote sensing image scene classification: Benchmark and state of the art," *Proc. IEEE*, vol. 105, no. 10, pp. 1865–1883, 2017.
- [27] B. Zhang, Y. Zhang, and S. Wang, "A lightweight and discriminative model for remote sensing scene classification with multidilation pooling module," *IEEE J. Sel. Topics Appl. Earth Observ. Remote Sens.*, vol. 12, no. 8, pp. 2636–2653, 2019.
- [28] M. Sandler, A. Howard, M. Zhu, A. Zhmoginov, and L.-C. Chen, "Mobilenetv2: Inverted residuals and linear bottlenecks," in *IEEE Comput. Vis. Pattern Recog.*, 2018, pp. 4510–4520.
- [29] C. Xu, G. Zhu, and J. Shu, "A lightweight and robust lie group-convolutional neural networks joint representation for remote sensing scene classification," *IEEE Trans. Geosci. Remote Sens.*, vol. 60, pp. 1–15, 2021.
- [30] J. Wang, W. Li, M. Zhang, and J. Chanussot, "Large kernel sparse convnet weighted by multi-frequency attention for remote sensing scene understanding," *IEEE Trans. Geosci. Remote Sens.*, vol. 61, pp. 1–12, 2023.
- [31] R. Girshick, J. Donahue, T. Darrell, and J. Malik, "Rich feature hierarchies for accurate object detection and semantic segmentation," in *IEEE Comput. Vis. Pattern Recog.*, 2014, pp. 580–587.
- [32] J. Long, E. Shelhamer, and T. Darrell, "Fully convolutional networks for semantic segmentation," in *IEEE Comput. Vis. Pattern Recog.*, 2015, pp. 3431–3440.
- [33] K. He, X. Zhang, S. Ren, and J. Sun, "Deep residual learning for image recognition," in *IEEE Comput. Vis. Pattern Recog.*, 2016, pp. 770–778.
- [34] W. Lu, S.-B. Chen, J. Tang, C. H. Ding, and B. Luo, "A robust feature downsampling module for remote sensing visual tasks," *IEEE Trans. Geosci. Remote Sens.*, vol. 61, pp. 1–12, 2023.
- [35] D. Hendrycks and K. Gimpel, "Gaussian error linear units (gelus)," *arXiv preprint arXiv:1606.08415*, 2016.
- [36] V. Nair and G. E. Hinton, "Rectified linear units improve restricted boltzmann machines," in *Int. Conf. Mach. Learn.*, 2010, pp. 807–814.
- [37] X. Ma, X. Dai, Y. Bai, Y. Wang, and Y. Fu, "Rewrite the stars," in *IEEE Comput. Vis. Pattern Recog.*, 2024.
- [38] J. Pan, A. Bulat, F. Tan, X. Zhu, L. Dudziak, H. Li, G. Tzimiropoulos, and B. Martinez, "Edgevits: Competing light-weight cnns on mobile devices with vision transformers," in *Eur. Conf. Comput. Vis.*, 2022, pp. 294–311.
- [39] M. Maaz, A. Shaker, H. Cholakkal, S. Khan, S. W. Zamir, R. M. Anwer, and F. Shahbaz Khan, "Edgenext: Efficiently amalgamated cnn-transformer architecture for mobile vision applications," in *Eur. Conf. Comput. Vis. Worksh.*, 2022, pp. 3–20.
- [40] S. Mehta and M. Rastegari, "Mobilevit: light-weight, general-purpose, and mobile-friendly vision transformer," *arXiv preprint arXiv:2110.02178*, 2021.
- [41] W. Wang, E. Xie, X. Li, D.-P. Fan, K. Song, D. Liang, T. Lu, P. Luo, and L. Shao, "Pvt v2: Improved baselines with pyramid vision transformer," *Comput. Vis. Media*, vol. 8, no. 3, pp. 415–424, 2022.
- [42] Y. Li, Q. Hou, Z. Zheng, M.-M. Cheng, J. Yang, and X. Li, "Large selective kernel network for remote sensing object detection," in *IEEE Int. Conf. Comput. Vis.*, 2023, pp. 16794–16805.
- [43] X. Cai, Q. Lai, Y. Wang, W. Wang, Z. Sun, and Y. Yao, "Poly kernel inception network for remote sensing detection," in *IEEE Comput. Vis. Pattern Recog.*, 2024.
- [44] J. Deng, W. Dong, R. Socher, L.-J. Li, K. Li, and L. Fei-Fei, "Imagenet: A large-scale hierarchical image database," in *IEEE Comput. Vis. Pattern Recog.*, 2009, pp. 248–255.
- [45] G.-S. Xia, X. Bai, J. Ding, Z. Zhu, S. Belongie, J. Luo, M. Datcu, M. Pelillo, and L. Zhang, "Dota: A large-scale dataset for object detection in aerial images," in *IEEE Comput. Vis. Pattern Recog.*, 2018, pp. 3974–3983.
- [46] J. Ding, N. Xue, Y. Long, G.-S. Xia, and Q. Lu, "Learning roi transformer for oriented object detection in aerial images," in *IEEE Comput. Vis. Pattern Recog.*, 2019, pp. 2849–2858.
- [47] Y. Xu, M. Fu, Q. Wang, Y. Wang, K. Chen, G.-S. Xia, and X. Bai, "Gliding vertex on the horizontal bounding box for multi-oriented object detection," *IEEE Trans. Pattern Anal. Mach. Intell.*, vol. 43, no. 4, pp. 1452–1459, 2020.
- [48] C. Xu, J. Ding, J. Wang, W. Yang, H. Yu, L. Yu, and G.-S. Xia, "Dynamic coarse-to-fine learning for oriented tiny object detection," in *IEEE Comput. Vis. Pattern Recog.*, 2023, pp. 7318–7328.
- [49] G. Cheng, J. Wang, K. Li, X. Xie, C. Lang, Y. Yao, and J. Han, "Anchor-free oriented proposal generator for object detection," *IEEE Trans. Geosci. Remote Sens.*, vol. 60, pp. 1–11, 2022.
- [50] J. Han, J. Ding, N. Xue, and G.-S. Xia, "Redet: A rotation-equivariant detector for aerial object detection," in *IEEE Comput. Vis. Pattern Recog.*, 2021, pp. 2786–2795.
- [51] X. Xie, G. Cheng, J. Wang, X. Yao, and J. Han, "Oriented r-cnn for object detection," in *IEEE Int. Conf. Comput. Vis.*, 2021, pp. 3520–3529.
- [52] Y. Pu, Y. Wang, Z. Xia, Y. Han, Y. Wang, W. Gan, Z. Wang, S. Song, and G. Huang, "Adaptive rotated convolution for rotated object detection," in *IEEE Int. Conf. Comput. Vis.*, 2023, pp. 6589–6600.
- [53] D. Wang, J. Zhang, B. Du, G.-S. Xia, and D. Tao, "An empirical study of remote sensing pretraining," *IEEE Trans. Geosci. Remote Sens.*, 2022.
- [54] W. Lu, S.-B. Chen, Q.-L. Shu, J. Tang, and B. Luo, "Decouplet: A lightweight backbone network with efficient feature decoupling for remote sensing visual tasks," *IEEE Trans. Geosci. Remote Sens.*, vol. 62, pp. 1–13, 2024.
- [55] I. Loshchilov and F. Hutter, "Decoupled weight decay regularization," in *Int. Conf. Learn. Represent.*, 2019.
- [56] E. D. Cubuk, B. Zoph, J. Shlens, and Q. V. Le, "Randaugment: Practical automated data augmentation with a reduced search space," in *IEEE Comput. Vis. Pattern Recog.*, 2020, pp. 702–703.
- [57] W. Li, Y. Chen, K. Hu, and J. Zhu, "Oriented reppoints for aerial object detection," in *IEEE Comput. Vis. Pattern Recog.*, 2022, pp. 1829–1838.
- [58] K. Li, G. Wan, G. Cheng, L. Meng, and J. Han, "Object detection in optical remote sensing images: A survey and a new benchmark," *ISPRS J. Photogramm. Remote Sens.*, vol. 159, pp. 296–307, 2020.
- [59] A. Paszke, S. Gross, F. Massa, A. Lerer, J. Bradbury, G. Chanan, T. Killeen, Z. Lin, N. Gimelshein, L. Antiga *et al.*, "Pytorch: An imperative style, high-performance deep learning library," in *Neur. Inf. Proc. Syst.*, vol. 32, 2019.
- [60] M. Oršić and S. Šegvić, "Efficient semantic segmentation with pyramid fusion," *Pattern Recog.*, vol. 110, p. 107611, 2021.
- [61] C. Yu, J. Wang, C. Peng, C. Gao, G. Yu, and N. Sang, "Bisenet: Bilateral segmentation network for real-time semantic segmentation," in *Eur. Conf. Comput. Vis.*, 2018, pp. 325–341.
- [62] R. Li, S. Zheng, C. Zhang, C. Duan, J. Su, L. Wang, and P. M. Atkinson, "Multiattention network for semantic segmentation of fine-resolution remote sensing images," *IEEE Trans. Geosci. Remote Sens.*, vol. 60, pp. 1–13, 2021.
- [63] A. Srinivas, T.-Y. Lin, N. Parmar, J. Shlens, P. Abbeel, and A. Vaswani, "Bottleneck transformers for visual recognition," in *IEEE Comput. Vis. Pattern Recog.*, 2021, pp. 16519–16529.
- [64] R. Li, S. Zheng, C. Zhang, C. Duan, L. Wang, and P. M. Atkinson, "Abcnnet: Attentive bilateral contextual network for efficient semantic segmentation of fine-resolution remotely sensed imagery," *ISPRS J. Photogramm. Remote Sens.*, vol. 181, pp. 84–98, 2021.
- [65] W. Xu, Y. Xu, T. Chang, and Z. Tu, "Co-scale conv-attentional image transformers," in *IEEE Int. Conf. Comput. Vis.*, 2021, pp. 9981–9990.
- [66] E. Xie, W. Wang, Z. Yu, A. Anandkumar, J. M. Alvarez, and P. Luo, "Segformer: Simple and efficient design for semantic segmentation with transformers," in *Neur. Inf. Proc. Syst.*, vol. 34, 2021, pp. 12077–12090.
- [67] J. Wang, Z. Zheng, X. Lu, and Y. Zhong, "Loveda: A remote sensing land-cover dataset for domain adaptive semantic segmentation," in *Conf. on Neur. Inf. Proc. Syst. Datasets and Benchmarks Track*, 2021.
- [68] Z. Zheng, Y. Zhong, J. Wang, and A. Ma, "Foreground-aware relation network for geospatial object segmentation in high spatial resolution remote sensing imagery," in *IEEE Comput. Vis. Pattern Recog.*, 2020, pp. 4096–4105.
- [69] R. Strudel, R. Garcia, I. Laptev, and C. Schmid, "Segmenter: Transformer for semantic segmentation," in *IEEE Int. Conf. Comput. Vis.*, 2021, pp. 7262–7272.
- [70] T. Xiao, Y. Liu, B. Zhou, Y. Jiang, and J. Sun, "Unified perceptual parsing for scene understanding," in *Eur. Conf. Comput. Vis.*, 2018, pp. 418–434.
- [71] A. Ma, J. Wang, Y. Zhong, and Z. Zheng, "Factseg: Foreground activation-driven small object semantic segmentation in large-scale remote sensing imagery," *IEEE Trans. Geosci. Remote Sens.*, vol. 60, pp. 1–16, 2022.
- [72] R. Xu, C. Wang, J. Zhang, S. Xu, W. Meng, and X. Zhang, "Rssformer: Foreground saliency enhancement for remote sensing land-cover segmentation," *IEEE Trans. Image Proc.*, vol. 32, pp. 1052–1064, 2023.
- [73] J. Wang, Y. Zhong, A. Ma, Z. Zheng, Y. Wan, and L. Zhang, "Lovenas: Towards multi-scene land-cover mapping via hierarchical searching adaptive network," *ISPRS J. Photogramm. Remote Sens.*, vol. 209, pp. 265–278, 2024.

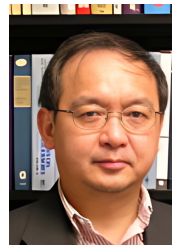
- [74] H. Chen and Z. Shi, "A spatial-temporal attention-based method and a new dataset for remote sensing image change detection," *Remote Sens.*, vol. 12, no. 10, p. 1662, 2020.
- [75] S. Ji, S. Wei, and M. Lu, "Fully convolutional networks for multisource building extraction from an open aerial and satellite imagery data set," *IEEE Trans. Geosci. Remote Sens.*, vol. 57, no. 1, pp. 574–586, 2018.
- [76] M. Lebedev, Y. V. Vizilter, O. Vygolov, V. A. Knyaz, and A. Y. Rubis, "Change detection in remote sensing images using conditional adversarial networks," *The International Archives of the Photogrammetry, Remote Sensing and Spatial Information Sciences*, vol. 42, pp. 565–571, 2018.
- [77] Q. Shi, M. Liu, S. Li, X. Liu, F. Wang, and L. Zhang, "A deeply supervised attention metric-based network and an open aerial image dataset for remote sensing change detection," *IEEE Trans. Geosci. Remote Sens.*, vol. 60, pp. 1–16, 2021.
- [78] C. Zhang, P. Yue, D. Tapete, L. Jiang, B. Shangguan, L. Huang, and G. Liu, "A deeply supervised image fusion network for change detection in high resolution bi-temporal remote sensing images," *ISPRS J. Photogramm. Remote Sens.*, vol. 166, pp. 183–200, 2020.
- [79] H. Chen, Z. Qi, and Z. Shi, "Remote sensing image change detection with transformers," *IEEE Trans. Geosci. Remote Sens.*, vol. 60, pp. 1–14, 2022.
- [80] W. G. C. Bandara and V. M. Patel, "A transformer-based siamese network for change detection," in *Int'l Geosci. Remote Sens. Symp.*, 2022, pp. 207–210.
- [81] Y. Feng, H. Xu, J. Jiang, H. Liu, and J. Zheng, "Icif-net: Intra-scale cross-interaction and inter-scale feature fusion network for bitemporal remote sensing images change detection," *IEEE Trans. Geosci. Remote Sens.*, vol. 60, pp. 1–13, 2022.
- [82] Y. Feng, J. Jiang, H. Xu, and J. Zheng, "Change detection on remote sensing images using dual-branch multilevel intertemporal network," *IEEE Trans. Geosci. Remote Sens.*, vol. 61, pp. 1–15, 2023.
- [83] Z.-H. You, J.-X. Wang, S.-B. Chen, C. H. Ding, G.-Z. Wang, J. Tang, and B. Luo, "Crossed siamese vision graph neural network for remote sensing image change detection," *IEEE Trans. Geosci. Remote Sens.*, vol. 61, pp. 1–16, 2023.
- [84] Z. Li, C. Tang, X. Liu, W. Zhang, J. Dou, L. Wang, and A. Y. Zomaya, "Lightweight remote sensing change detection with progressive feature aggregation and supervised attention," *IEEE Trans. Geosci. Remote Sens.*, vol. 61, pp. 1–12, 2023.
- [85] G. Wang, G. Cheng, P. Zhou, and J. Han, "Cross-level attentive feature aggregation for change detection," *IEEE Trans. Circuit Syst. Video Technol.*, 2023.



Wei Lu received the B.Eng. degree from Fuyang Normal University, China in 2020. He is currently pursuing a Ph.D. in computer science from Anhui University, Hefei, China. His current research interests include image processing, efficient AI, low-level visual tasks, and remote sensing.



Si-Bao Chen received the B.S. and M.S. degrees in probability and statistics and the Ph.D. degree in computer science from Anhui University of China in 2000, 2003, and 2006, respectively. From 2006 to 2008, he was a Postdoctoral Researcher at the University of Science and Technology of China. Since 2008, he has been a teacher at Anhui University. From 2014 to 2015, he was a visiting scholar at the University of Texas in Arlington. His current research interests include image processing, pattern recognition, machine learning and computer vision.



Chris H.Q. Ding obtained his Ph.D. from Columbia University in 1987. He has held positions at the California Institute of Technology, Jet Propulsion Laboratory, Lawrence Berkeley National Laboratory, University of California, and the University of Texas in Arlington. Since 2021, he has been affiliated with the Chinese University of Hong Kong, Shenzhen. Dr. Ding is an expert in machine learning, data mining, bioinformatics, information retrieval, web link analysis, and high-performance computing. His works were cited over 60,000 times (Google scholar).



Jin Tang received the B.Eng. degree in automation and the Ph.D. degree in computer science from Anhui University, Hefei, China, in 1999 and 2007, respectively. He is currently a Professor with the School of Computer Science and Technology, Anhui University. His current research interests include computer vision, pattern recognition, machine learning, and deep learning.



Bin Luo received the B.Eng. degree in electronics and the M.Eng. degree in computer science from Anhui University, Hefei, China, in 1984 and 1991, respectively, and the Ph.D. degree in computer science from the University of York, York, U.K., in 2002. From 2000 to 2004, he was a Research Associate with the University of York. He is currently a Professor with Anhui University. His current research interests include graph spectral analysis, image and graph matching, statistical pattern recognition, digital watermarking, and information security.